J Mater Sci (2024) 59:20–37

Ceramics

Wear behavior at high temperature of ZrO_2–Y_2O_3 (YSZ) plasma-sprayed coatings

D. Franco[1,2,*], F. Vargas[1], E. López[1], and H. Ageorges[2]

[1] GIPIMME-GIMACYR Research Groups, University of Antioquia, Medellín, Colombia
[2] ECNRS, IRCER, UMR7315, University of Limoges, 87000 Limoges, France

Received: 26 July 2023
Accepted: 26 November 2023
Published online: 20 December 2023

ABSTRACT

The wear behavior of two plasma-sprayed zirconia–yttria coatings was studied at high temperatures. Agglomerated and sintered, as well as fused and crushed zirconia–yttria feedstock powders were used to manufacture bimodal and monomodal coatings by atmospheric plasma spraying onto an INCONEL 718 substrate previously coated with a NiCrAlY bond coat. The structure of the coatings was analyzed by SEM on their cross section and surface. The samples were subjected to wear conditions by sliding contact through a ball-on-disk test up to 1000 °C, using an alumina ball 6 mm in diameter as the counterbody, on which a load of 5 N was applied. The samples were rotated during 20000 cycles, reaching a speed of 0.10 $m \cdot s^{-1}$ at the contact area with the counterbody. The porosity, phase, and mechanical properties were determined before and after wear tests. The results indicate that at 25 °C, both coatings have enough mechanical resistance to withstand the tribological conditions they were exposed to. Therefore, low wear rates were produced by ductile deformation. The tribological conditions became more aggressive as the thermal stresses increased with the test temperature, producing cracking, and detaching particles in the coatings tested at 500 and 750 °C. Consequently, high wear rates related to brittle deformation were obtained. However, the transformation of the amorphous phase to the *t*′-zirconia phase, produced at 1000 °C, increased the hardness of both coatings and, consequently, their wear resistance; thus, the predominant mechanism of damage was ductile deformation, with wear rates similar to those obtained when the coatings were tested at 25 °C.

Introduction

Atmospheric plasma-sprayed (APS) zirconia–yttria top coatings deposited on NiCrAlY bond coats have been widely used as thermal barrier coatings (TBCs) for gas turbine blades and combustion system components owing to their high thermal stability, low thermal conductivity, and relatively large thermal expansion, which is close to that of a metallic substrate [1–3]. Under operating conditions, TBCs are exposed to

Handling Editor: David Cann.

Address correspondence to E-mail: idavid.franco@udea.edu.co

https://doi.org/10.1007/s10853-023-09204-w

high-temperature oxidation, hot corrosion, and severe wear, such as erosion, adhesion, abrasion, and fretting [3].

The mechanisms and chemical reactions that produce high-temperature oxidation and hot corrosion of yttria-stabilized zirconia (YSZ) TBCs manufactured by APS have been studied to identify ways to improve their performance and useful life [4–7]. Recently, studies have been conducted to understand the tribological behavior of atmospheric-pressure plasma-sprayed YSZ thermal barrier coatings exposed to conditions similar to those in operation. Specifically, D. Shin et al. [8] have evaluated the erosion resistance of these coatings at temperatures between 537 and 980 °C, using an erosion tunnel to simulate the modern gas turbine operating conditions. The erodent particles were transported by gas at velocities between 122 and 305 $m \cdot s^{-1}$, impacting the coating surface at angles between 20° and 90°. The effect of the coating structure porosity (porosities of 12.9 ± 0.5% and 19.5 ± 1.2%) on the erosion resistance was evaluated. These results demonstrate that higher wear rates due to erosion are associated with increased porosity in the YSZ coatings [8].

Similarly, Pakseresht et al. [3] studied the wear behavior of atmospheric plasma-sprayed YSZ coatings manufactured from Metco 204NS powder, with and without the addition of alumina whiskers, using a ball-on-disk microtribometer at room temperature to promote abrasive conditions on the contact surface between the coating and counterbody. An alumina ball with a diameter of 5 mm was used as the counterbody, on which normal loads of 7, 10, and 13 N were applied for each test. During the tests, the samples were rotated at a linear speed of 0.5 $m \cdot s^{-1}$ up to a sliding distance of 500 m. The wear track analysis reported by the authors indicated that a smooth surface and abrasive detachment of particles were produced with wear rates between 4.1×10^{-2} and 7.3×10^{-2} $mm^3/N \cdot m$ for the coating without adding alumina whiskers and between 3.5×10^{-2} and 5.3×10^{-2} $mm^3/N \cdot m$ for specimens reinforced with alumina whiskers [3].

Liang et al. [9], Pawlowski [10], Shi et al. [11], Xiao et al. [12], and Lima et al. [13] reported that plasma thermally sprayed coatings using nanometric and submicrometric feedstock powders improved the mechanical properties by improving the coating's structure. Additionally, H. Chen et al. [14] reported better wear performance of zirconia coatings manufactured from nanometric feedstock powders than that of the coatings sprayed from micrometric powders, which was attributed in the same way to the optimization of their structure, and therefore, the improvement of their mechanical properties.

L. Bai et al. [15–17] studied the tribological performance of YSZ coatings exposed to sliding contact with an alumina ball from 25 to 800 °C. The results obtained by these researchers showed that the alumina ball used as a counterpart produces severe wear on the surface of these coatings, not only at room temperature [17], but also up to 800 °C [16]. Likewise, the results of these studies show that as the test temperature increases, the rate of coating wear tends to increase. However, the formation of a tribolayer produced on the surface of the coatings when they were tested at temperatures above 200 °C protects them from the damage produced by the alumina counterpart, reducing their wear rate [15, 16].

The topcoats of thermal barrier coatings are frequently manufactured by atmospheric plasma spraying from yttria-stabilized zirconia powders, which were previously fused and crushed, or agglomerated and sintered, using powder processing methods. Although fused and crushed powders are usually less expensive, agglomerated and sintered powders are commonly used to manufacture coatings that are exposed to high temperatures because their bimodal structure gives them higher thermal shock resistance than the monomodal structure obtained in coatings sprayed from fused and crushed powders [18]. At room temperature, the mechanical properties (hardness, elastic modulus, and fracture toughness) of monomodal and bimodal structure YSZ coatings could be statistically similar [19]. The phase transformations at high temperatures could change the mechanical performance of these coatings. Additionally, the yttria content used in the feedstock powders plays an essential role in the stability of the t'-ZrO_2 phase when zirconia-based materials are exposed to high temperatures for a long time. It has been reported that the complete and maximum stability of the t'-ZrO_2 phase is achieved when the content of Y_2O_3 is above 6 wt% [20].

A few studies have reported the performance of these coatings exposed to sliding contact with an alumina ball at temperatures up to 800 °C [16, 17]. However, their behavior at higher temperatures have not yet been published. For this reason, this work studied the wear performance of YSZ coatings exposed to abrasive conditions at temperatures between 25 and 1000 °C. The coatings studied were manufactured by atmospheric plasma spraying from agglomerated and

sintered, as well as fused and crushed ZrO_2–Y_2O_3 feedstock powders, to produce bimodal and monomodal microstructures, respectively, which are specified for thermal barrier coatings in aircraft, stationary gas turbines, and engines with high thermal shock resistance, thermal insulating properties, and hot corrosion resistance [21].

Materials and methods

To prepare the substrates, an INCONEL 718 bar was cut into discs with a diameter of 25 mm and a height of 7 mm. The surface to be coated was blasted using a corundum jet of particles, reaching an arithmetic average roughness (Ra) between 4 and 10 µm. Subsequently, the substrates were sonicated in an acetone bath to remove residues from the treatment previously carried out with abrasive particles and other dirt. NiCrAlY Sulzer–Metco Amdry 962™ powder was atmospheric plasma sprayed as a bond coat on an INCONEL 718 substrate. Afterward, ZrO_2–Y_2O_3 top coatings were also manufactured by APS from the agglomerated and sintered H.C. Starck Amperit 827.423™ and fused and crushed H.C. Starck Amperit 825™ powders to produce bimodal and monomodal microstructures, respectively. The bond and top coatings are manufactured using a Sulzer–Metco PTF4™ plasma torch according to the parameters listed in Table 1. These parameters were selected from preliminary tests carried out looking for coatings with the crystalline and amorphous phases, as well as the mechanical properties usually required for their use as topcoat in thermal barriers.

The chemical compositions of the feedstock powders were measured using a wavelength-dispersive X-ray fluorescence (WD-XRF) spectrometer with commercial reference: Thermo Fisher SCIENTIFIC ARL™ OPTIM'X. In the same way, Horiba PARTITA LA-950V2 laser diffraction (LD) equipment was used to characterize the particle size distribution of these powders. The crystallographic composition of the feedstock powders and the coatings was determined using an X-ray Cu Kα 1 radiation (DRX) Diffractometer with commercial reference: Bruker D8 ADVANCE and the X'Pert Highscore Plus Software following the COD cards: (1) t'-ZrO_2 (1525706), (2) c-ZrO_2 (1521753), and (3) m-ZrO_2 (1010912). Afterward, the Rietveld method was used to quantify the phases, following the same COD cards and the Material Analysis Using Diffraction (MAUD) software. In addition, a JEOL JSM IT-300 LV scanning electronic microscopy (SEM) equipment was used to characterize the morphological features of the ZrO_2–Y_2O_3 feedstock powders particles, the surfaces, and the cross sections of the coatings, as well as the surface of wear tracks. The surfaces and the cross sections of the coatings were

Table 1 Plasma-spraying parameters

Parameter	Top coating powders		Bond coating powder
	H.C. Starck Amperit 827.423™	H.C. Starck Amperit 825.1™	Sulzer–Metco Amdry 962™
Current intensity [A]	650	650	650
Ar-H_2 flow rate [L/min]	45-15	45–15	45-15
Nozzle internal diameter [mm]	7	7	7
Feeder type	Screw Praxair	Screw Praxair	Screw Praxair
Powder flow rate [g/min]	22–28	24–30	15–19
Ar carrier gas pressure [bar]	5.0	5.0	5.0
Ar carrier gas flow rate [L/min]	4.5	4.5	4.5
Spraying distance [mm]	100 ± 1	100 ± 1	100 ± 1
Sample translation speed [mm/s]	24	24	24
Sample rotation speed [rpm]	124	124	124
Cooling air distance [mm]	12	12	12
Preheating temperature [°C]	300	300	300
Surface substrate preheating passes	5–8	5–8	2–3
Spraying time [min]	4	4	2
Number of spraying passes	95	93	55

ground and polished according to the ASTM E1920 standard [22] to obtain an arithmetic average roughness (Ra) lower than 0.2 μm. The porosity was determined on the cross sections of the coatings from images taken by SEM according to the indications of the ASTM E2109 standard [23] and using the Image J software. On the other hand, the hardness, the elastic modulus, and the fracture toughness of the YSZ coatings were determined from indentations performed on the polished surfaces of all samples using a Shimadzu HMV-G20 equipment following the specifications of ASTM C-1327 [24] and ASTM E-384 [25] standards. The hardness, the elastic modulus, and the fracture toughness were calculated according to Eqs. (1)–(3), respectively:

$$H_V = 0.0018544\frac{P_N}{d^2} \tag{1}$$

where H_V is the Vickers microhardness [GPa], P_N is the normal load applied to the indenter [N], and d is the average length of the two diagonals produced during indentation [mm].

$$E = \frac{-\alpha H_K}{\left(\frac{b'}{a'} - \frac{b}{a}\right)} \tag{2}$$

where E is Young's modulus [GPa], α is a constant ($\alpha = 0.45$), H_k is the Knoop microhardness [Pa], a' and b' are the longer and shorter diagonals, respectively, produced by the indentation [μm], and a and b are the geometric constants of the indenter ($b/a = 1/7.11$), as in Fig. 1a.

$$K_{IC} = 0.0016\sqrt{\frac{E}{H}}\frac{P_N}{C^{3/2}} \tag{3}$$

where K_{IC} is the fracture toughness [MPa·m$^{1/2}$],E is the Young's modulus [GPa], H is the Vickers microhardness [GPa], P_N is the applied normal load on the indenter [N], and C is the longest radial crack produced during the indentation [mm], as shown in Fig. 1b.

Wear tests were performed at 25, 500, 750, and 1000 °C using a ball-on-disk tribometer under dry sliding contact without eliminating the formed debris. An alumina ball 6 mm in diameter, with a hardness Vickers of 18.0 ± 0.5 GPa, was used as a counter-body, on which a normal load of 5 N was applied. The samples were rotated during 20000 cycles reaching a relative linear speed of 0.1 m·s^{-1} with respect to the alumina ball, according to some recommendations of the ASTM G-99 standard [26]. Morphological characterization of the wear tracks produced during the tribological tests was performed using SEM with the aforementioned equipment. The wear rate was calculated from the profile curves of the wear tracks measured on the samples (Fig. 2) using a Surtronic S125 profilometer and Eq. (4).

$$WR_{Sample} = \frac{\text{Volumen}}{\text{Load} \times \text{Distance}} = \frac{A_s 2\pi r_{wt}}{1000 P_N N_c 2\pi r_{wt}} \tag{4}$$

where WR_{Sample} denotes the wear rate [mm^3/N·m],A_s is the wear track cross-sectional area [μm^2], r_{wt} is the radius of the wear track [mm], P_N is the applied normal load [N]; and N_c is the total number of cycles.

In the same way, to calculate the wear rate produced for each counter-body, an electronic micrometer with commercial reference: Mitutoyo and Eq. (5) were used.

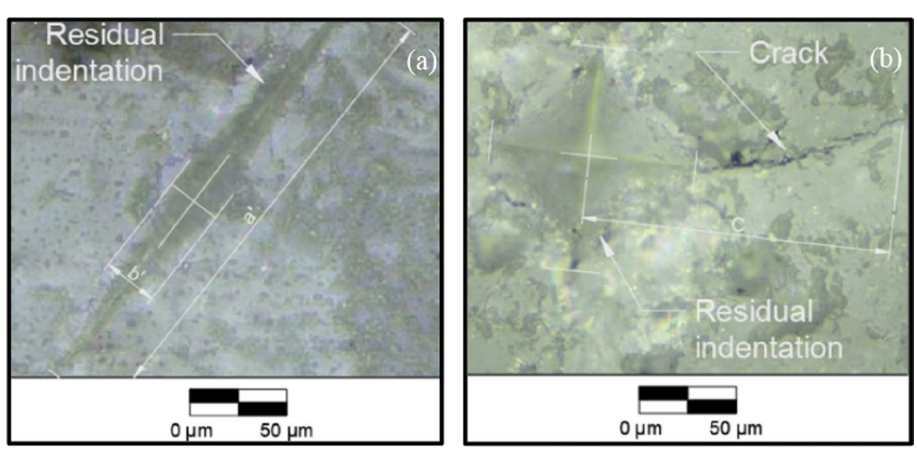

Figure 1 Typical indentation to determine: **a** Elastic modulus and **b** fracture toughness.

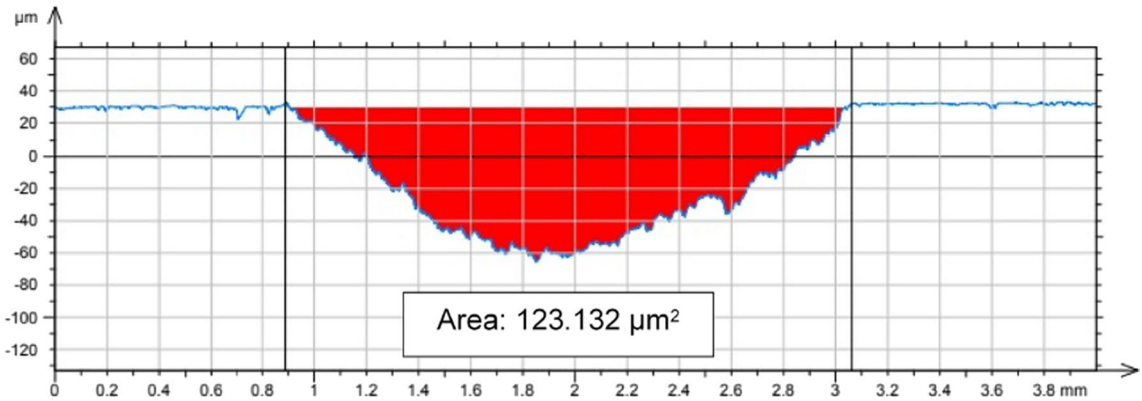

Figure 2 Typical cross section of the wear track's profile obtained on the coatings tested.

$$WR_{Counterbody} = \frac{\text{Volumen}}{\text{Load} \times \text{Distance}} = \frac{\frac{1}{3}\pi h^2(3R - h)}{P_N D_T} \quad (5)$$

where $WR_{Counterbody}$ is the wear rate [mm^3/N·m], h is the spherical cap height [mm], R is the radius of the counter-body [mm], P_N is the normal load applied [N], and D_T is the total distance of the test [m].

After the wear tests, the porosity, crystallographic phases, hardness, elastic modulus, and fracture toughness were reevaluated using the same equipment, standards, and equations mentioned above to compare the values with those obtained before the wear tests. The porosity, mechanical properties, and worn area were measured for three samples, ten times each, guaranteeing statistical reproducibility and repeatability for all measurements.

Results

Feedstock powder characterization

The results of the chemical analysis, the particle size distribution, and the morphological characterization carried out on the Sulzer–Metco Amdry 962™ powder used to manufacture the bond coating indicated that it was composed of Ni (~ 67.0 wt%), Cr (~ 22.0 wt%), Al (~ 10.0 wt%), and Y (~ 1.0 wt%), its particle size distribution is between d_{10} = 63.59 and d_{90} = 121.73 µm, and its geometry is spheroidal typical of the atomized powders [27]. The results of the chemical analysis carried out on the feedstock powders used to manufacture the top coatings showed that both the H.C. Starck Amperit 827.423™ powder and the H.C. Starck Amperit 825™ powder were composed mainly of ZrO_2 and Y_2O_3 with Al_2O_3, Na_2O, K_2O, TiO_2, NiO, MgO, CaO, Fe_2O_3, and HfO_2 in quantities lower than 0.5 wt%. Regarding the particle size distribution, the H.C. Starck Amperit 827.423™ powder is significantly coarser (d_{10} = 20.51 and d_{90} = 83.17 µm) than the fused and crushed one (d_{10} = 24.39 and d_{90} = 49.67 µm). The results of the chemical analyses, phases, and particle size distributions of the powders used to produce the top coatings are listed in Table 2.

The amounts of yttria in the H.C. Starck Amperit 827.423™ powder and the H.C. Starck Amperit 825™ one are 3.21 and 8.60 wt%, respectively, which were enough to stabilize the 63.1 wt% and 93.5 wt% of tetragonal phase (t'-ZrO_2) in these powders, respectively. The t'-ZrO_2 is the characteristic phase of YSZ thermal barrier coatings. For this reason, most of the TBCs are yttria-stabilized zirconia containing ≈ 6.0–8.0 wt% of Y_2O_3 [28, 29]. It is important to note that under equilibrium conditions, yttria stabilizes a tetragonal phase above about 1050 °C [29]

The morphological analysis of these powders allowed us to identify that H.C. Starck Amperit 827.423™ corresponds to spherical granules composed of sub-micrometric particles with nanoparticles in them, as well as some pores on their surface, as manufactured by agglomeration and sintering processes [27, 30]. In contrast, H.C. Starck Amperit 825™ comprises particles with irregular morphology and fracture patterns, characteristic of fused and crushed powders [27]. The morphologies of these powders are shown in Fig. 3a, b.

The agglomerated and sintered, and the fused and crushed ZrO_2–Y_2O_3 powders are widely used to manufacture thermal barrier coatings by APS [31, 32]. In order to identify the coatings manufactured from both

Table 2 Physicochemical features of the feedstock powders

Properties		H.C. Starck Amperit 827.423™	H.C. Starck Amperit 825.1™
Chemical composition (wt%)	ZrO_2	93.89 ± 0.51	84.90 ± 0.55
	Y_2O_3	3.21 ± 0.62	8.60 ± 0.58
	SiO_2	1.21 0.08	3.19 ± 0.07
	Al_2O_3	0.46 ± 0.05	0.14 ± 0.06
	CaO	0.13 ± 0.01	0.15 ± 0.01
	TiO_2	0.11 ± 0.01	0.11 ± 0.01
	Na_2O	0.08 ± 0.01	0.28 ± 0.02
	K_2O	–	0.14 ± 0.09
	Fe_2O_3	0.06 ± 0.01	0.06 ± 0.01
	NiO	–	0.18 ± 0.01
	MgO	–	0.11 ± 0.01
	HfO_2	0.66 ± 0.13	2.05 ± 0.33
	Others*	0.19 ± 0.05	0.09 ± 0.01
Phase analysis (wt%)	t'-ZrO_2	63.1 ± 8.3	93.5 ± 3.8
	m-ZrO_2	32.4 ± 1.3	–
	YZr_8O_{14}	4.5 ± 0.3	–
	Amorphous	–	6.5 ± 0.4
Particle size distritubtion (μm)	d_{10}	20.51	24.39
	d_{50}	51.81	34.92
	d_{90}	93.17	49.67

*Others: In_2O_3, WO_3, Bi_2O_3, and Ga_2O_3

the agglomerated and sintered powder H. C. Starck Amperit 827.423™ and the fused and crushed H. C. Starck Amperit 825™, they were codified as $C_{A–S}$ and $C_{F–C}$, respectively.

Structural characterization of coatings

The structural analysis performed on the surfaces of both the $C_{A–S}$ and $C_{F–C}$ coatings revealed stacking of micrometrical splats, with some pores typical of thermally sprayed coatings [27, 33] (Fig. 4a, b). These porosities were produced mainly by discontinuities among the splats and were slightly more evident in the $C_{A–S}$ coating owing to the partially molten particles present in this sample [33]. It is essential to mention that these partially melted particles contain both submicrometric and nanometric particles, which gives these samples the features of a bimodal structure coating [33]. However, the cross-sectional structure showed good stacking among the lamellas and a homogenous interface between the top and bond coatings (Fig. 4c, d). The thicknesses and porosities of both coatings are listed in Table 3.

For both coatings, the porosity values before and after the wear tests at the different temperatures evaluated are statistically the same (all p-values are > 0.05), indicating that they do not experience sintering processes. Partially molten particles identified on both the surface and the cross section of $C_{A–S}$ coating are due to the granules of submicrometric and nanometric particles agglomerated and sintered and their consequent low heat transfer when they fly in the plasma jet [33].

Crystallographic characterization

The results of the XRD analysis performed on the manufactured coatings are shown in Fig. 5a, b, and the results of the quantification of phases identified are presented in Table 4. In Fig. 5a, b, the background of the XRD spectra was eliminated in order to compare among the results obtained for each sample tested at different temperatures. The diffraction peaks as well as the broadening and the hump evidenced ~ 30° indicate that both coatings were composed mainly of t'-ZrO_2 and the amorphous phase (> 50.0 wt% and > 30.0 wt%, respectively). In addition, lower quantities of m-ZrO_2 and c-ZrO_2 phases were identified. The broadening and hump in the diffraction peak ~ 30° were previously reported by other authors [34, 35].

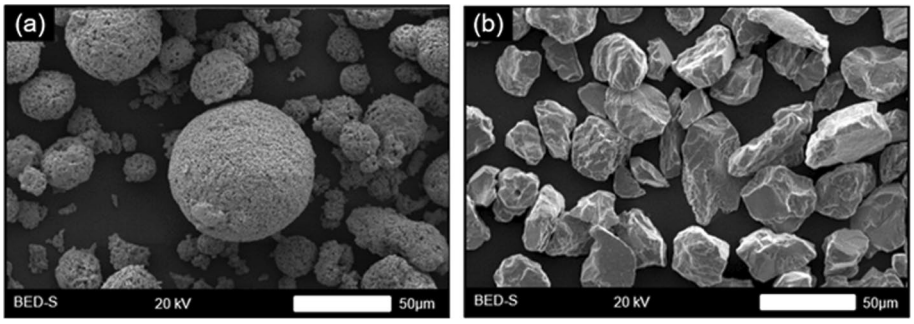

Figure 3 Morphology of ZrO_2–Y_2O_3 feedstock powders: **a** H.C. Starck Amperit 827.423™ and **b** H.C. Starck Amperit 825™.

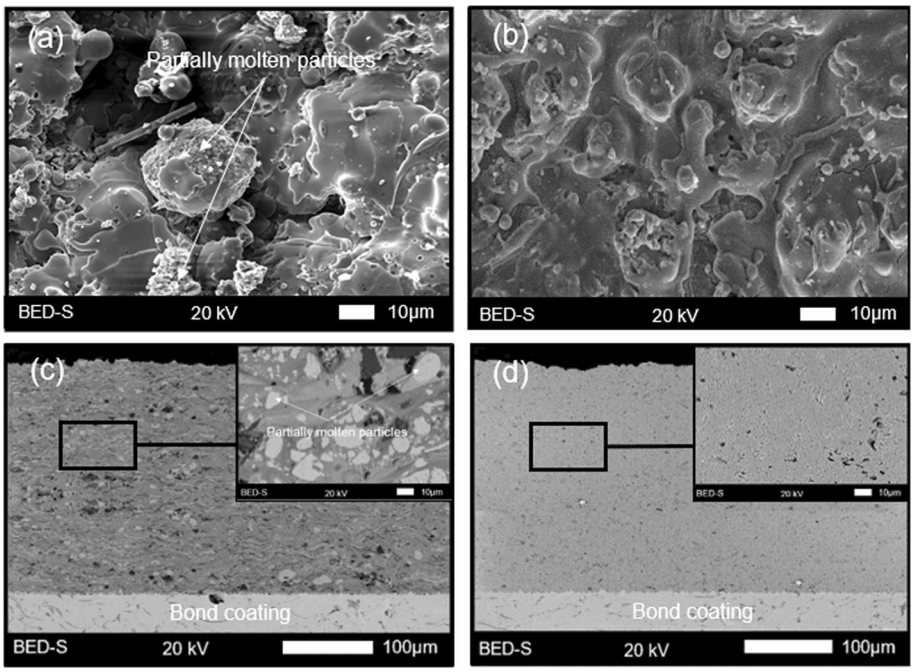

Figure 4 As-sprayed structure of the ZrO_2–Y_2O_3 coatings. Surface: **a** $C_{A–S}$ coating and **b** $C_{F–C}$ coating. Cross section: **c** $C_{A–S}$ coating and **d** $C_{F–C}$ coating.

Table 3 Thickness and porosity of both ZrO_2–Y_2O_3 coatings

Sample	Thickness [μm]	Wear tests temperature [°C]	Porosity before wear tests [%]	Porosity after wear tests [%]	ANOVA *p*-value
$C_{A–S}$ coating	275 ± 20	25	6.6 ± 1.2	6.5 ± 0.7	0.823
		500		6.5 ± 0.5	0.812
		750		6.4 ± 1.1	0.702
		1000		6.6 ± 0.7	1.000
$C_{F–C}$ coating	273 ± 22	25	5.9 ± 0.7	5.9 ± 0.9	1.000
		500		6.0 ± 0.4	0.701
		750		5.9 ± 0.9	1.000
		1000		5.9 ± 1.1	1.000

The m-ZrO_2 and c-ZrO_2 phases did not change significantly at different temperatures when the wear tests were performed ($p > 0.05$). On the other hand, from Table 4 is possible to see for both coatings that statistically, the quantities of the t'-ZrO_2 phase and the amorphous phase were steady after the wear test carried out at 25, 500, and 750 °C (p-value > 0.05). However, after the wear tests performed at 1000 °C, the t'-ZrO_2 phase increased, and the amorphous phase decreased (p-values < 0.005). It is important to note that other researchers have indicated that owing to the high cooling rate of particles deposited by atmospheric plasma spraying, the tetragonal phase obtained in the structure of coatings manufactured from ZrO_2–Y_2O_3 powders is a metastable phase, called the tetragonal-prime phase (t'-ZrO_2) [26, 35–38]. For this reason, in this study, the notation t'-ZrO_2 phase is used to refer to the t-ZrO_2 phase.

Mechanical characterization

The mechanical properties determined before and after the tribological tests are presented in Table 5. Generally, the hardness of both coatings measured at room temperature is similar, and statistically significant changes were not identified (p-value > 0.05) after the wear test carried up to 750 °C. However, the hardness of both coatings after the wear test carried out at 1000 °C increased (p-value < 0.05) with the increase of the t'-ZrO_2 phase, which could be produced by the

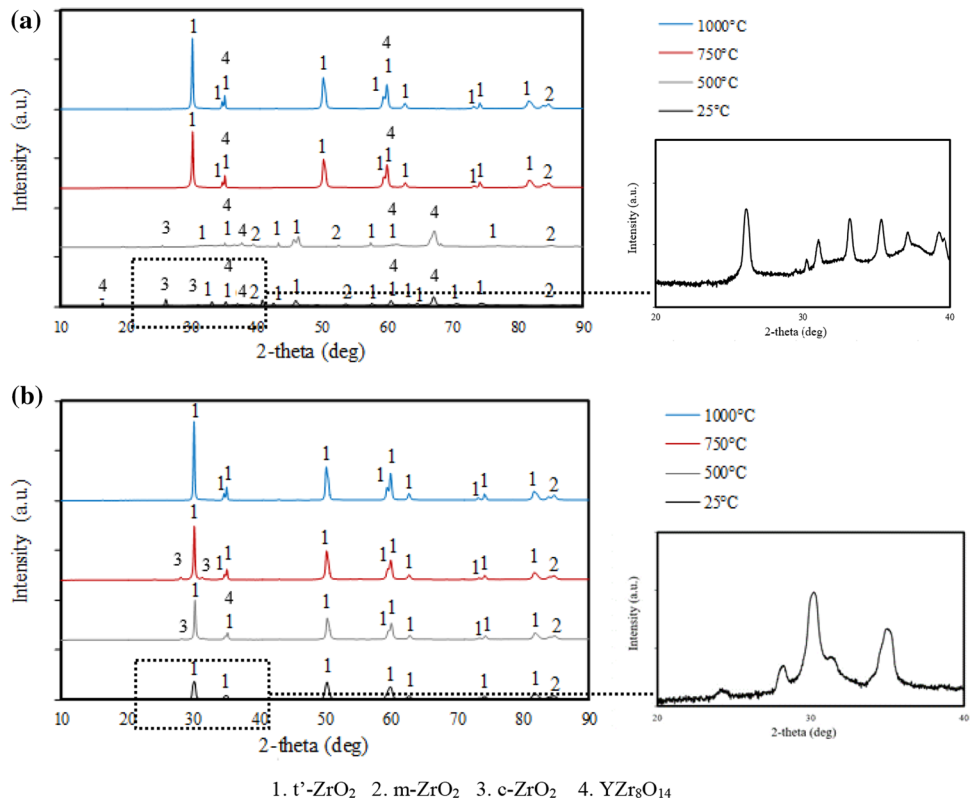

Figure 5 XRD patterns of the ZrO_2–Y_2O_3 coatings: **a** $C_{A–S}$ coating and **b** $C_{F–C}$ coating.

crystallization of the amorphous phase during the wear tests performed at this temperature. The materials based in the t-ZrO_2 phase have a higher hardness (~ 12.0 GPa) [38] than that of ZrO_2-based materials, which also have an amorphous phase (~ 8.5 GPa) [39, 40].

It is also possible to see in Table 5 that at all temperatures evaluated, the values of fracture toughness for the $C_{A–S}$ coating are slightly higher than those for the $C_{F–C}$ coating, as well as that at 1000 °C, the value of fracture toughness for the $C_{A–S}$ coatings remained without any change (p-value > 0.05), while this value in the $C_{F–C}$ coatings decreased (p-value < 0.05), which could be related to the presence of partially melted particles in the $C_{A–S}$ coating. Regarding Young's modulus values, these did not show statistically significant changes (p-value > 0.05) during the wear tests at all temperatures evaluated.

Tribological characterization

The wear track analysis of both YSZ coatings (Fig. 6a–p) demonstrated the development of different tribological mechanisms depending on the test temperature. In particular, both coatings have shown fuzzy wear tracks with friction marks and some slight spalling (Fig. 6a–d) after the tribological tests performed at 25 °C. Although the wear track of the coatings tested at 500 °C remains diffuse, the analysis performed at higher magnifications revealed the onset of both cracks and particle detachment from the coating (Fig. 6e–h), which are more evident on the samples tested at 750 °C in which the wear tracks are clearly evidenced (Fig. 6i–l). Other authors have reported comparable results with the occurrence of grooves and spalling pits in YSZ coatings exposed to tribological conditions similar to those used for the test performed at 500 °C, as well as delamination and ejection of wear particles owing to brittle fracture in coating performed at 800 °C [16]. Furthermore, regular wear tracks were observed in both coatings tested at 1000 °C and in a continuous layer consisting of debris particles where the plastic flow was identified (Fig. 6m–p).

The wear rate results are presented in Fig. 7a. They evidenced that the samples tested at 25 °C showed the lowest wear rate. In comparison, at 500 and 750 °C, the wear rates increased with the tribological test temperatures. Similar results were reported by other authors for YSZ coatings manufactured by APS and tested under similar tribological conditions

Table 4 Crystallographic phases in both ZrO_2–Y_2O_3 coatings before and after wear tests

Sample	Phases	Wear tests temperature [°C]	Before wear tests [wt%]	After wear tests [wt%]	ANOVA *p*-value
$C_{A–S}$ coating	*t*′-ZrO_2	25	51.6 ± 1.82	51.8 ± 1.4	0.723
		500		51.1 ± 1.9	0.597
		750		51.4 ± 1.2	0.852
		1000		77.2 ± 1.0	0.000
	m-ZrO_2	25	1.6 ± 0.8	1.8 ± 0.3	0.370
		500		1.1 ± 0.2	0.124
		750		1.4 ± 0.3	0.644
		1000		1.2 ± 0.3	0.204
	c-ZrO_2	25	2.5 ± 0.7	2.5 ± 0.7	1.000
		500		2.5 ± 0.5	0.943
		750		2.5 ± 0.5	0.860
		1000		2.7 ± 0.7	0.706
	YZr_8O_{14}	25	2.6 ± 0.5	2.8 ± 0.7	0.527
		500		2.9 ± 0.9	0.429
		750		2.8 ± 0.9	0.566
		1000		2.7 ± 0.9	0.785
	Amorphous	25	41.7 ± 1.3	41.0 ± 2.8	0.488
		500		42.4 ± 2.0	0.403
		750		41.9 ± 2.3	0.885
		1000		16.3 ± 2.4	0.000
$C_{F–C}$ coating	*t*′-ZrO_2	25	52.7 ± 1.4	52.8 ± 1.4	0.875
		500		52.1 ± 1.9	0.433
		750		52.4 ± 1.2	0.614
		1000		78.2 ± 1.0	0.000
	m-ZrO_2	25	1.6 ± 0.8	1.5 ± 0.3	0.718
		500		1.6 ± 0.2	1.000
		750		1.5 ± 0.4	0.729
		1000		1.4 ± 0.3	0.475
	c-ZrO_2	25	2.1 ± 0.5	2.0 ± 0.6	0.691
		500		2.0 ± 0.4	0.628
		750		2.1 ± 0.4	1.000
		1000		1.8 ± 0.5	0.196
	Amorphous	25	43.6 ± 2.9	43.7 ± 3.5	0.945
		500		44.3 ± 3.9	0.655
		750		44.0 ± 3.2	0.773
		1000		21.2 ± 3.1	0.000

[16]. For the samples tested at 1000 °C, the wear rates were decreased and showed values lower than those at 500 and 750 °C. For its part, Fig. 7b presents the wear rates produced on alumina counterbodies used to wear both coatings, showing an increase in the wear rate with the test temperature.

From Fig. 8a–h, it is possible to identify traces of friction on the worn counterbody surfaces, which is typical of abrasive wear, with no signs of wear by adhesion with the surface of coatings.

The friction coefficient values shown in Fig. 9, measured during the tribological tests for both coatings, increased with the increase of temperature until 750 °C. Then, they decreased for the samples evaluated at 1000 °C.

Table 5 Mechanical properties of both ZrO_2–Y_2O_3 coatings measured before and after the wear tests

Sample	Mechanical property	Wear tests temperature [°C]	Before wear tests [wt%]	After wear tests [wt%]	ANOVA *p*-value
$C_{A–S}$ coating	Hardness [GPa]	25	8.7 ± 0.5	8.3 ± 0.4	0.291
		500		8.5 ± 0.5	1.000
		750		8.8 ± 0.5	0.185
		1000		9.2 ± 0.5	0.041
	Young's modulus [GPa]	25	82 ± 16	87 ± 7	0.399
		500		79 ± 18	0.680
		750		71 ± 16	0.115
		1000		79 ± 13	0.558
	Fracture toughness [MPa·m$^{1/2}$]	25	3.2 ± 0.1	3.2 ± 0.1	1.000
		500		3.2 ± 0.1	1.000
		750		3.1 ± 0.2	0.181
		1000		3.1 ± 0.2	0.181
$C_{F–C}$ coating	Hardness [GPa]	25	8.7 ± 0.6	8.5 ± 0.6	0.445
		500		8.5 ± 0.5	0.561
		750		8.6 ± 0.5	0.695
		1000		9.3 ± 0.4	0.024
	Young's modulus [GPa]	25	90 ± 14	98 ± 12	0.210
		500		101 ± 13	0.099
		750		95 ± 19	0.556
		1000		95 ± 11	0.386
	Fracture toughness [MPa·m$^{1/2}$]	25	2.9 ± 0.1	3.0 ± 0.4	0.456
		500		2.8 ± 0.3	0.379
		750		2.7 ± 0.4	0.161
		1000		2.6 ± 0.4	0.032

Discussion

In ceramic materials, as YSZ coatings manufactured by APS, the tribological performance is influenced mainly by their hardness and fracture toughness [41, 42], which depend, among other factors, on the crystalline and amorphous phases of which they are composed. It is important to note in Table 4, the increase of the t'-ZrO_2 phase at the expense of the amorphous phase after the wear tests developed at 1000 °C (p-value < 0.05), which other researchers have previously reported, but for Al_2O_3–ZrO_2 plasma sprayed coatings [43]. However, the quantity of the m-ZrO_2 and c-ZrO_2 phases did not change with the heating of the samples during the tribological tests at high temperatures. This could be linked to both the temperature and time at which these tests were carried out are not enough for the transformation of these phases. During the tribological evaluation, the samples were exposed to each test temperature for 4 h, which could be insufficient for the diffusion of an additional amount of Y_2O_3 in the t'-ZrO_2 phase, as well as for Y_2O_3 diffusion from t'-ZrO_2 to produce a mixture of stable tetragonal phases with monoclinic or cubic phases. Other authors have reported the transformation of t'-ZrO_2 to m-ZrO_2 in ZrO_2-8 wt% Y_2O_3 coatings manufactured by APS and heated at 1100 °C for more than 800 h [20], as well as the transformation from t'-ZrO_2 to c-ZrO_2 in a single crystal of similar chemical composition heated at 1600 °C during 50 h [44]. Likewise, it has been reported that the transformation from t'-ZrO_2 to m-ZrO_2 in coatings manufactured by APS from powders with less than 6 wt% Y_2O_3 occurred slowly at 1300 °C [20]. In this order of ideas, since the m-ZrO_2 and c-ZrO_2 phases did not change and any decrease in porosity of the coatings was evidenced by sintering during tribological tests (Table 3), it was possible to establish that the key for the good wear behavior of coatings tested at 1000 °C, was the transformation from amorphous to t'-ZrO_2 phase,

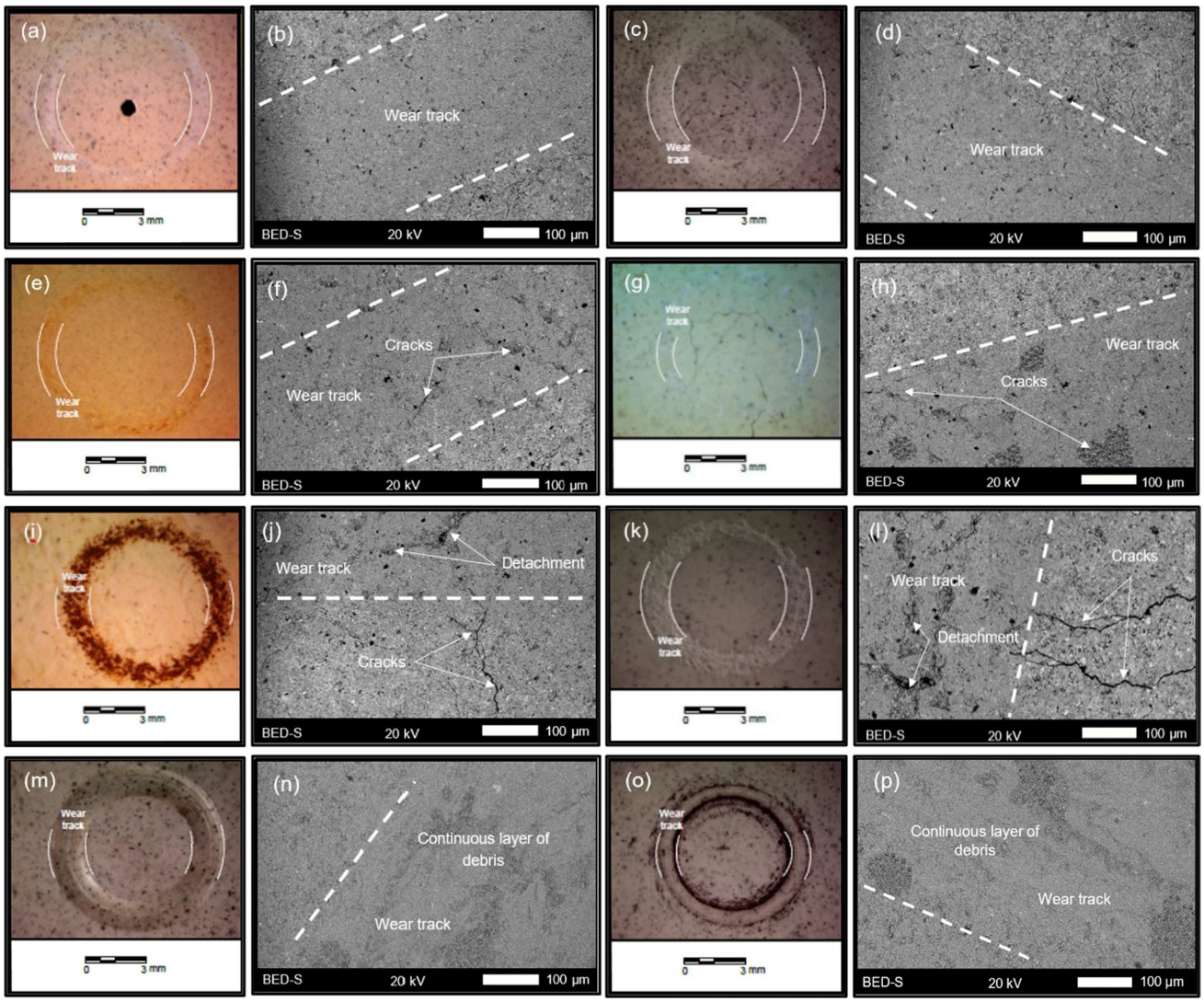

Figure 6 Typical wear tracks obtained in both ZrO_2–Y_2O_3 coatings tested at 25 °C: **a**, **b** $C_{A–S}$, **c**, **d** $C_{F–C}$, at 500 °C: **e**, **f** $C_{A–S}$, **g**, **h** $C_{F–C}$, at 750 °C: **i**, **j** $C_{A–S}$, **k**, **l** $C_{F–C}$, and at 1000 °C: **m**, **n** $C_{A–S}$, **o**, **p** $C_{F–C}$.

thanks the higher hardness of this crystalline phase regarding the amorphous one [45].

The fracture toughness of the $C_{A–S}$ coating was slightly higher than that of the $C_{F–C}$ coating at all the temperatures evaluated. This indicates that the fine particles remaining inside the partially molten granules detected in the structure of the $C_{A–S}$ coating (Fig. 4a) can relax the stress and then arrest the cracks produced by the microindentations carried out to measure this mechanical property, as reported by other authors [18, 46]. Additionally, the fracture toughness of the $C_{A–S}$ coating remained constant after the wear tests performed at different temperatures. At the same time, for the $C_{F–C}$ coating, this property decreased slightly after the wear test was carried out at 1000 °C. Although in Eq. (3), the increase in microhardness (H) could promote the decrease in the E/H ratio, the decrease in the crack length ($C^{3/2}$) owing to the presence of partially molten particles in the $C_{A–S}$ coating, in turn prompted an increase in the $P_N/C^{3/2}$ ratio, maintaining the fracture toughness at the end. On the other hand, in the $C_{F–C}$ coating, the absence of partially molten particles in its structure does not allow the reduction of the E/H ratio to be compensated by the increase of the $P_N/C^{3/2}$ ratio, due to the reduction of crack length after the tribological test carried out at 1000 °C.

The typical tribological mechanisms of ceramic materials under sliding contact conditions are

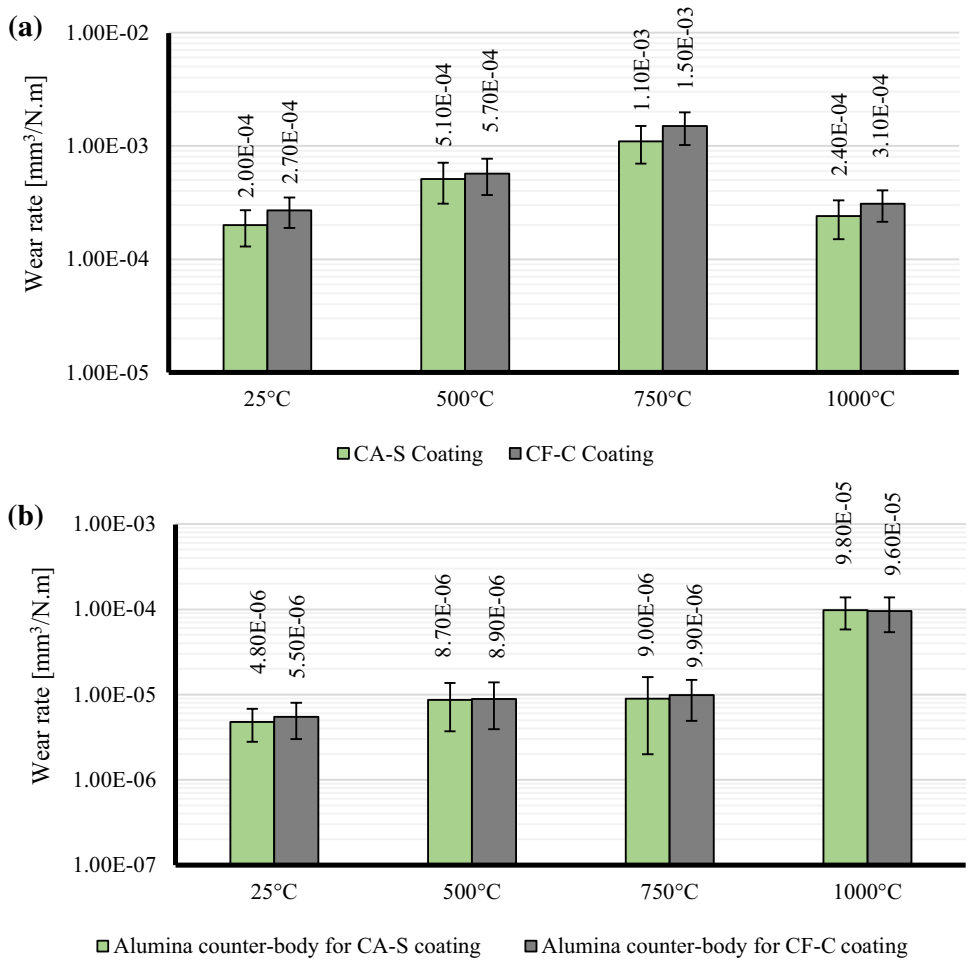

Figure 7 Wear rate of **a** coatings and **b** counterbodies.

functions of speed and load [46]. It is essential to highlight that when a ceramic material can withstand the mechanical stress applied by the counterbody, it produces a wear mechanism called "ductile deformation," which usually shows features such as friction marks, and plastic flow, and, therefore, low wear rates, as obtained for coatings tested at 25 and 1000 °C [47]. Moreover, suppose the ceramic material cannot withstand the mechanical stress applied by the counterbody. In that case, it produces another wear mechanism called "brittle deformation," which typically shows features such as fracture, cracks, and excessive detachment of particles, and therefore, high wear rates, as obtained for coatings tested at 500 and 750 °C [47]. Ductile and brittle deformation are wear mechanisms applicable only to ceramic materials [47].

It is important to note that despite using two powders with different chemical compositions (especially in terms of Y_2O_3 content) and morphologies, the results in Table 4–5 show that the manufactured coatings have similarities in the type and percentage of crystalline and amorphous phases, as well as in their mechanical properties, which gives them similar tribological behaviors at each temperature evaluated. However, this does not rule out a possible difference between the two types of coatings if they are evaluated at high temperatures for longer durations. In the coating manufactured from the powder containing 3 wt% Y_2O_3, the t'-ZrO_2 phase could reach a transformation to the m-ZrO_2 phase [37], while in that containing 8 wt% Y_2O_3, the t'-ZrO_2 phase will be completely stable [20]. Thus, it is possible to establish that the decrease in the wear resistance of the two coatings is due to the increase in thermal stress with the temperature of the tests, promoting cracks and the detachment of particles by brittle deformation. However, when the two coatings were tested at 1000 °C, the amorphous to t'-ZrO_2 phase transformation occurred. Their hardness increased, and a protective debris layer was produced, promoting the wear by ductile deformation.

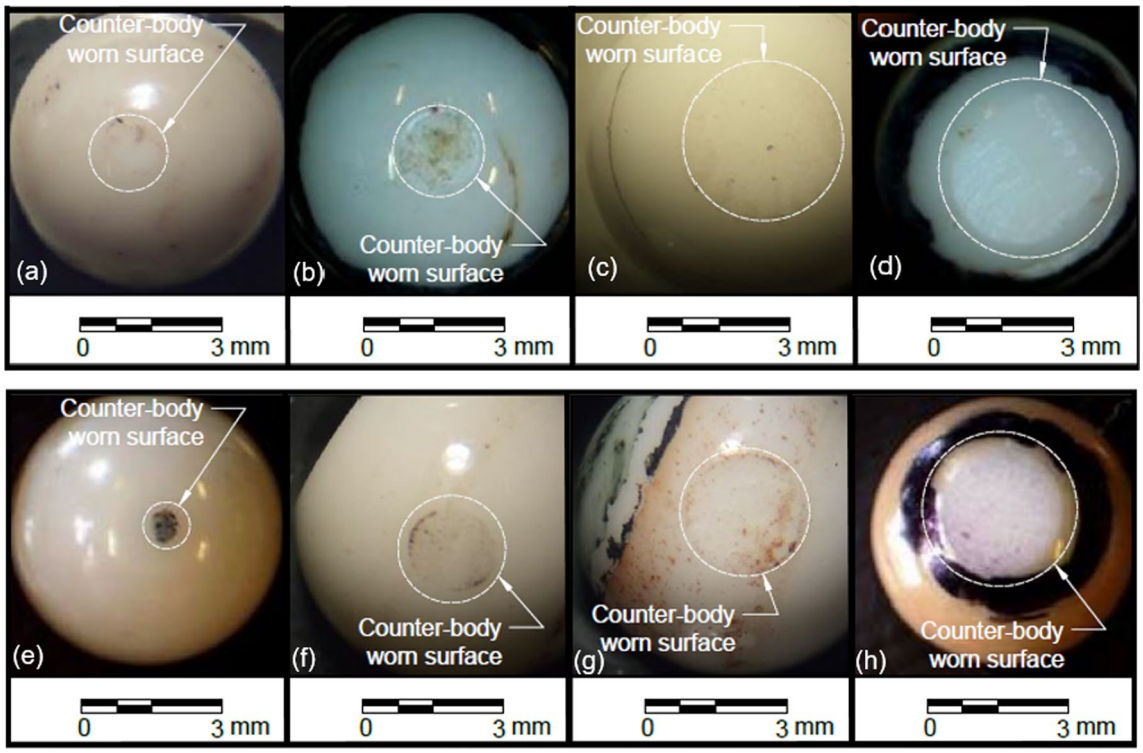

Figure 8 Typical wear on the counter-bodies used to test the ZrO_2–Y_2O_3 coatings. Alumina counter-body/C_{A-S} coating pair at: **a** 25 °C, **b** 500 °C, **c** 750 °C, and **d** 1000 °C. Alumina counter-body/C_{F-C} coating pair at: **e** 25 °C, **f** 500 °C, **g** 750 °C, and **h** 1000 °C.

Figure 9 Friction coefficients measured during the wear tests at different temperatures.

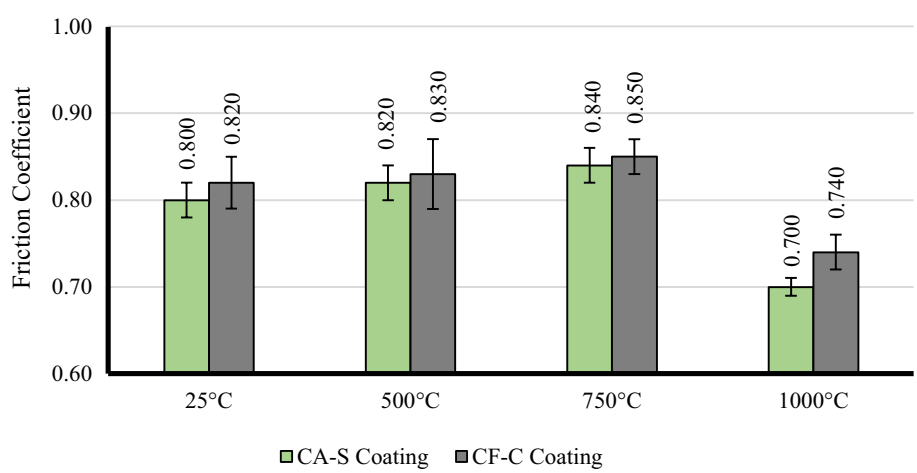

The particle detachment evidenced on the wear tracks of samples tested at 500 °C, which was more notorious for the coating performed at 750 °C, is characteristic of wear produced by brittle deformation because the stresses applied by the hard alumina ball (~ 19 GPa) used as a counterbody during sliding contact are substantially higher than the mechanical resistance of the coatings, whose hardness is ~ 9 GPa and their fracture toughness is 2.9–3.2 MPa·m$^{1/2}$ [47]. On the other hand, the microcracks produced by the sliding of the counterbody on the surface of the samples are due to fatigue fracture, as has been previously reported by other authors [48, 49]. These cracks were more evident in the samples tested at 500 and 750 °C owing to the thermal stresses produced as the test temperature increased. In the coatings tested at 1000 °C, the fine debris could have decreased the stress contact between their surface and the alumina counterbody

[50] and produced a continuous layer densified by this contact.

The transformation of the wear mechanism from ductile deformation produced at room temperature to brittle deformation at temperatures up to 800 °C was reported by J. H. Ouyang et al. [48] for ZrO_2–Y_2O_3 coatings manufactured by low-pressure plasma spraying; however, the new transformation of wear mechanism toward ductile deformation occurring at 1000 °C that is presented in this study for ZrO_2–Y_2O_3 coatings manufactured by atmospheric plasma spraying is unpublished. This transformation from wear by brittle deformation produced in the samples tested between 500 and 750 °C to wear by ductile deformation at 1000 °C (Fig. 6m–p) was mainly due to the increase in hardness produced by the crystallization of the amorphous phase, as well as the formation of a protective layer from debris. Figure 6n–p indicates the protective layer produced on the wear tracks of coatings tested at 1000 °C, evidenced by plastic flow described by other authors for wear with ductile deformation [47].

From Fig. 6a–p, it is possible to see similar wear behaviors for both coatings, starting with wear by ductile deformation, followed by wear by fragile deformation, and finally wear by ductile deformation. These wear behaviors have been reported in [51, 52] for ZrO_2–Al_2O_3 and Al_2O_3 coatings, respectively. It is also important to note that the wear rate values reported in Fig. 7a are comparable to those reported in [16] for YSZ coatings tested at similar tribological conditions at 25 and 500 °C, as well as those reported in [51, 52] at high temperatures for Al_2O_3 and Al_2O_3–ZrO_2 coatings, respectively.

As shown in Fig. 7a, the samples tested at 25 °C showed the lowest wear rate, which was likely due to the slight damage caused by ductile deformation during the tribological contact between the surface of the coating, the alumina ball, and the low quantity of debris (Fig. 6a–d). At 500 and 750 °C, the wear rates increased with the tribological test temperatures, probably because of the contribution of thermal stresses to the wear tests (Fig. 6e–l). For the samples tested at 1000 °C, the wear rate was lower than that at 500 °C and 750 °C, probably due to the reduction in the severity of the tribological contact promoted by the protective layer formed from debris. In the same way, Fig. 7b shows the increase of the counterbodies wear rates as the temperature increased in all samples (Fig. 8a–h), which was probably related to: (i) the hardness decrease of alumina ball when exposed to high temperatures [53], (ii) the increase in the severity of the contact conditions due to the increase in thermal stresses, and (iii) the increase of hardness in both coatings heated at 1000 °C owing to their crystallographic changes mentioned above.

The highest wear rate in the alumina ball used as the counter-body in tests performed at 1000 °C confirms that the increase in the hardness of the coatings was a driving factor for the change in the wear mechanism from brittle deformation at 750 °C to ductile deformation at 1000 °C. Wear-by-ductile deformation occurs when the tested material has sufficient mechanical resistance to withstand the contact conditions to which it is exposed, and a controlled quantity of rounded debris produces a layer that protects the sample [47, 50]. However, it can increase the severity of the damage produced to the counter-body by harder particles. The decrease in the friction coefficient measured in the tests performed at 1000 °C indicated that the debris that acted as a third body tended to be more rounded than those produced in the tests performed at 500 and 750 °C, where the wear was due to brittle deformation.

The friction coefficient values (Fig. 9) measured during the tribological tests for both coatings increased with the temperature increase until 750 °C. They then decreased for the samples evaluated at 1000 °C, which could be linked to the fine particles of debris in the protective layer, whose morphology tended to be mainly spherical, thus reducing this coefficient. The obtained coefficients of friction were similar to those previously reported for YSZ and PSZ materials against alumina [16, 54].

Conclusions

- It was studied the wear behavior up to 1000 °C of two YSZ coatings widely used to manufacture thermal barrier coatings, which were manufactured by APS from both an agglomerated and sintered, and a fused and crushed ZrO_2–Y_2O_3 feedstock powders aiming to produce bimodal and monomodal microstructures, respectively. The wear behavior is correlated with the mechanical properties, which depend on the crystalline phases. The results allowed us to identify the changes in the wear mechanism as a function of temperature.
- Both ZrO_2–Y_2O_3 coatings have shown no significant differences in their hardness before and after the wear tests up to 750 °C. However, the increase of the t'-ZrO_2 phase at the expense of the

amorphous phase during the tests performed at 1000 °C contributed to increasing the hardness and, therefore, the wear performances of the coatings. This increase in hardness prevented the severe cracking and particle detachment produced in the coatings tested at 500 and 750 °C due to high thermal stresses; therefore, only a limited amount of fine debris was produced, forming a protective layer on the contact surface of samples.
- The wear mechanisms identified in both atmospheric plasma sprayed ZrO_2–Y_2O_3 coatings were at 25 °C, ductile deformation, at 500 and 750 °C, brittle deformation, and at 1000 °C, ductile deformation again. This behavior in all the samples evaluated was strongly related to the thermal stresses and changes in their mechanical properties owing to their crystallographic phases.

Acknowledgements

The authors are grateful to Departamento Administrativo de Ciencia, Tecnologia e Innovacion—Colciencias—(Bogotá—Colombia). Convocatoria Doctorado Nacional—647 de 2014 for the Doctoral Fellowship, awarded to David Franco and the CODI-Committee of the University of Antioquia for its economic support given to both the GIPIMME—GIMMACYR research group in 2019 and for FIT 1-1-01 project.

Author contributions

Not Applicable.

Funding

Open Access funding provided by Colombia Consortium.

Data availability

Not Applicable.

Declarations

Conflict of interest The authors declare that they have no known competing financial interests or personal relationships or conflict of interests that could have appeared to influence the work reported in this paper. The authors declare the following financial interests/personal relationships which may be considered as potential competing interests:

Ethical approval Not Applicable.

References

[1] Goto T (2013) A new thick film coating technology-laser chemical vapor deposition, handbook of advanced ceramics. In: materials, applications, processing, and properties, 2nd edn. https://doi.org/10.1016/B978-0-12-385469-8.00045-9

[2] Sai Sahith M, Giridhara G, Suresh Kumar R (2018) Development and analysis of thermal barrier coatings on gas turbine blades—a review. Mater Today Proc 5(1):2746–2751. https://doi.org/10.1016/j.matpr.2018.01.060

[3] Pakseresht H, Saremi M, Omidvar H, Alizadeh M (2019) Micro-structural study and wear resistance of thermal barrier coating reinforced by alumina whisker. Surf Coat Technol 366:338–348. https://doi.org/10.1016/j.surfcoat.2019.03.059

[4] Dong TS, Wang R, Di YL, Wang HD, Li GL, Fu BG (2019) Mechanism of high temperature oxidation resistance

improvement of double-layer thermal barrier coatings (TBCs) by La. Ceram Int 45(7):9126–9135. https://doi.org/10.1016/j.ceramint.2019.01.251

[5] Wang R, Dong TS, Di YI, Wang HD, Li GL, Liu L (2019) High temperature oxidation resistance and thermal growth oxides formation and growth mechanism of double-layer thermal barrier coatings. J Alloy Compd 798:773–783. https://doi.org/10.1016/j.jallcom.2019.05.052

[6] Soboyejo WO, Mensah P, Diwan R, Crowe J, Akwaboa S (2011) High temperature oxidation interfacial growth kinetics in YSZ thermal barrier coatings with bond coatings of. Mater Sci Eng A 528(6):2223–2230. https://doi.org/10.1016/j.msea.2010.11.066

[7] Habibi MH, Wang L, Guo SM (2012) Evolution of hot corrosion resistance of YSZ, $Gd_2Zr_2O_7$, and $Gd_2Zr_2O_7$ + YSZ composite thermal barrier coatings in Na_2SO_4 + V_2O_5 at 1050 °C. J Eur Ceram Soc 32(8):1635–1642. https://doi.org/10.1016/j.jeurceramsoc.2012.01.006

[8] Shin D, Hamed A (2018) Influence of micro-structure on erosion resistance of plasma sprayed 7YSZ thermal barrier coating under gas turbine operating conditions. Wear 396–397:34–47. https://doi.org/10.1016/j.wear.2017.11.005

[9] Liang B, Zhang G, Liao H, Coddet C, Ding C (2009) Friction and wear behavior of ZrO_2–Al_2O_3 composite coatings deposited by air plasma spraying: Correlation with physical and mechanical properties. Surf Coat Technol 203(20–21):3235–3242. https://doi.org/10.1016/j.surfcoat.2009.03.056

[10] Pawlowski L (2008) Finely grained nanometric and submicrometric coatings by thermal spraying: a review. Surf Coat Technol 202:4318–4328. https://doi.org/10.1016/j.surfcoat.2008.04.004

[11] Shi JY, Verweij H (2008) Preparation and characterization of nanostructured ZrO_2 coatings on dense and porous substrates. Thin Solid Films 516:3919–3923. https://doi.org/10.1016/j.tsf.2007.07.200

[12] Xiao F, Gong X, Liu S, Jia J, Zhang X, Wang L, Yan M, Wang Y (2022) A novel nanostructured mullite feedstock for environmental barrier coatings via atmosphere plasma spraying. Crystals 12:726. https://doi.org/10.3390/cryst12050726

[13] Lima RS, Marple BR (2005) Superior performance of high-velocity oxyfuel-sprayed nanostructured TiO_2 in comparison to air plasma-sprayed conventional Al_2O_3–$13TiO_2$. J Therm Spray Technol 14:397–404. https://doi.org/10.1361/105996305X59413

[14] Chen H, Zhang Y, Ding C (2002) Tribological properties of nanostructured zirconia coatings deposited by plasma spraying. Wear 253:885–893. https://doi.org/10.1016/S0043-1648(02)00221-1

[15] Bai L, Wan S, Yi G, Sun H (2022) Exploring the influences of the counterpart materials on friction and wear behaviors of atmospheric plasma-sprayed YSZ coating. Ceram Int 48(20):29601–29613. https://doi.org/10.1016/j.ceramint.2022.06.214

[16] Bai L, Zhang H, Wan S, Yi G, Sun H (2023) Tailoring wear and tribo-induced interaction of YSZ coating sliding against Si_3N4 and Al_2O_3 counterparts. Wear 518–519:204628. https://doi.org/10.1016/j.wear.2023.204628

[17] Bai L, Yi G, Wan S, Wang W, Sun H (2023) Comparison of tribological performances of plasma sprayed YSZ, YSZ/Ag, YSZ/MoO_3 and YSZ/Ag/MoO_3 coatings from 25 to 800 °C. Wear 526–527:204944. https://doi.org/10.1016/j.wear.2023.204944

[18] Jamali H, Mozafarinia R, Razavi RS, Ahmadi-Pidani R (2012) Comparison of thermal shock resistances of plasma-sprayed nanostructured and conventional yttria stabilized zirconia thermal barrier coatings. Ceram Int 38(8):6705–6712. https://doi.org/10.1016/j.ceramint.2012.05.060

[19] Wang L, Wang Y, Sun XG, He JQ, Pan ZY, Wang CH (2012) Microstructure and indentation mechanical properties of plasma sprayed nano-bimodal and conventional ZrO_2–8wt%Y_2O_3 thermal barrier coatings. Vacuum 86(8):1174–1185. https://doi.org/10.1016/j.vacuum.2011.10.029

[20] Brandon JR, Taylor R (1989) Thermal properties of ceria and yttria partially stabilized zirconia thermal barrier coatings. Surf Coat Technol 39–40(1):143–151. https://doi.org/10.1016/0257-8972(89)90049-2

[21] H. C. Starck, Amperit Thermal Spray Powders, Technical Sheet Data. http://tecnospray.net/download/HCST/AMPERIT-Brochure.pdf

[22] ASTM E-1920 (2003) Standard guide for metallographic preparation of thermal spraying coatings

[23] ASTM E-2109 (2014) Standard test methods for determining area percentage porosity in thermal sprayed coatings

[24] ASTM C-1327 (2015) Standard test method for vickers indentation hardness of advanced ceramics

[25] ASTM E-384 (2017) Standard test method for microindentation hardness of materials

[26] ASTM G-99 (2017) Standard test method for wear testing with a pin-on-disk apparatus

[27] Pawlowski L (1994) The science and engineering of thermal spray coatings. Wiley. https://doi.org/10.1002/9780470754085.ch3

[28] Chena S, Zhou X, Song W, Sun J, Zhang H, Jiang J, Deng L, Dong CX (2019) Mg_2SiO_4 as a novel thermal barrier coating material for gas turbine applications. J Eur Ceram

Soc 39(7):2397–2408. https://doi.org/10.1016/j.jeurceramsoc.2019.02.016

[29] Clarke DR, Levi CG (2003) Materials design for the next generation thermal barrier coatings. Annu Rev Mater Res 33:383–417. https://doi.org/10.1146/annurev.matsci.33.011403.113718

[30] Bertrand G, Roy P, Filiatre C, Coddet C (2005) Spray-dried ceramic powders: a quantitative correlation between slurry characteristics and shapes of the granules. Chem Eng Sci 60(1):95–102. https://doi.org/10.1016/j.ces.2004.04.042

[31] Höganäs, Thermal Spray Powders, Technical Sheet Data. https://www.hoganas.com/globalassets/download-media/sharepoint/brochures-and-datasheets---all-documents/surface-coating_thermal-spray-powders_2438hog.pdf?mode=brochure#page=10

[32] Oerlikon Metco, Thermal Spray Materials Guide, Technical Sheet Data, https://www.ahtstlab.com/wp-content/uploads/2021/05/ThermalSprayMaterialsGuide.pdf

[33] Fauchais PL, Heberlein JVR, Boulos MI (2014) Thermal spray fundamentals from powder to part. Springer. https://doi.org/10.1007/978-0-387-68991-3

[34] Ji Z, Allen Haynes J, Voelkl E, Michael Rigsbee J (2001) Phase formation and stability in reactively sputter deposited yttria-stabilized zirconia coatings. J Am Ceram Soc 84(5):929–936. https://doi.org/10.1111/j.1151-2916.2001.tb00770.x

[35] Muraleedharan K, Subrahmanyam J, Bhaduri SB (1988) Identification of t' phase in ZrO_2-7.5 wt% Y_2O_3 thermal-barrier coatings. J Am Ceram Soc 71(5):C226–C227. https://doi.org/10.1111/j.1151-2916.1988.tb05061.x

[36] Mauer G, Jarligo MO, Mack DE, Vaßen R (2013) Plasma—sprayed thermal barrier coatings: new materials, processing issues, and solutions. J Therm Spray Technol 22:646–658. https://doi.org/10.1007/s11666-013-9889-8

[37] Osorio JD, Lopera A, Toro A, Hernandez JP (2014) Phase transformations in air plasma-sprayed yttria-stabilized zirconia thermal barrier coatings. Dyna 81(185):13–18. https://doi.org/10.15446/dyna.v81n185.33409

[38] Dub SN, Gogotsi GA, Lomonova EE (1995) Hardness and fracture toughness of tetragonal zirconia single crystals. J Mater Sci Lett 14:46–49. https://doi.org/10.1007/BF02565283

[39] Gandhi AS, Jayaram V, Chokshi AH (1999) Dense amorphous zirconia–alumina by low-temperature consolidation of spray–pyrolyzed powders. J Am Ceram Soc 82(10):2613–2618. https://doi.org/10.1111/j.1151-2916.1999.tb02131.x

[40] Gust M, Goo G, Wolfenstine J, Mecartmy ML (1993) Influence of amorphous grain boundary phases on the superplastic behavior of 3-mol%-Yttria-stabilized tetragonal zirconia polycrystals (3Y-TZP). J Am Ceram Soc 76(7):1681–1690. https://doi.org/10.1111/j.1151-2916.1993.tb06635.x

[41] Hsu SM, Shen M (2004) Wear prediction of ceramics. Wear 256(9–10):867–878. https://doi.org/10.1016/j.wear.2003.11.002

[42] Le TH, Chae YH, Kim SS (2005) Sliding wear behavior of plasma sprayed zirconia ceramic coating under different conditions. World Tribol Congr III. https://doi.org/10.1115/WTC2005-63852

[43] Kim HJ, Kim YJ (1999) Amorphous phase formation of the pseudo-binary Al_2O_3–ZrO_2 alloy during plasma spray processing. J Mater Sci 34:29–33. https://doi.org/10.1023/A:1004492919174

[44] Lanteri V, Heuer AH, Mitchell TE (1985) Tetragonal phase in the system ZrO_2–Y_2O_3. J Am Ceram Soc 12:118–130

[45] Mecartney ML (1987) Influence of an amorphous second phase on the properties of yttria-stabilized tetragonal zirconia polycrystals (Y-TZP). J Am Ceram Soc 70(1):54–58. https://doi.org/10.1111/j.1151-2916.1987.tb04853.x

[46] Yang D, Gao Y, Liu H, Sun C (2017) Thermal shock resistance of bimodal structured thermal barrier coatings by atmospheric plasma spraying using nanostructured partially stabilized zirconia. Surf Coat Technol 315:9–16. https://doi.org/10.1016/j.surfcoat.2017.01.112

[47] Stachowiak GW, Batchelor A (2014) Engineering tribology. Butterworth Heinemann-Team LRN. https://doi.org/10.1016/C2011-0-07515-4

[48] Ouyang JH, Sasaki S (2002) Microstructure and tribological characteristics of ZrO_2–Y_2O_3 ceramic coatings deposited by laser-assisted plasma hybrid spraying. Tribol Int 35:255–264. https://doi.org/10.1016/S0301-679X(02)00005-1

[49] He Y, Winnubst L, Burggraaf AJ, Verweij H, Vander Varst PGT, De With B (2005) Influence of porosity on friction and wear of tetragonal zirconia polycrystal. J Am Ceram Soc 80(2):377–380. https://doi.org/10.1111/j.1151-2916.1997.tb02841.x

[50] Fischer TE, Zhu Z, Kim H, Shin DS (2000) Genesis and role of wear debris in sliding wear of ceramics. Wear 245:53–60. https://doi.org/10.1016/S0043-1648(00)00465-8

[51] Franco D, Ageorges H, Lopez E, Vargas F (2019) Tribological performance at high temperatures of alumina coatings applied by plasma spraying process onto a refractory material. Surf Coat Technol 371:276–286. https://doi.org/10.1016/j.surfcoat.2019.04.058

[52] Franco D, Ageorges H, Lopez E, Vargas F (2021) Wear behavior at high temperatures of ZrO_2–Al_2O_3 plasma sprayed coatings and an electro-melted AZS refractory.

Surf Coat Technol 425:127715. https://doi.org/10.1016/j.surfcoat.2021.127715

[53] Tingaud O, Bertrand P, Bertrand G (2010) Microstructure and tribological behavior of suspension plasma sprayed Al_2O_3 and Al_2O_3–YSZ composite coatings Microstructure and tribological behavior of suspension plasma sprayed Al_2O_3 and Al_2O_3–YSZ composite coatings. Surf Coat Technol 205:1004–1008. https://doi.org/10.1016/j.surfcoat.2010.06.003

[54] Yust S, Carignan FJ (2008) Observation on the sliding wear of ceramics. ASLE Trans 28:245–253. https://doi.org/10.1080/05698198508981618